Preparation of perovskite-like PbBiO$_2$I/g-C$_3$N$_4$ exhibiting visible-light-driven activity

Li-Wen Chen[a], Hung-Lin Chen[b], Chung-Shin Lu[c], Shiuh-Tsuen Huang[a], Tsung-Wen Yeh[a], Chiing-Chang Chen[a],*

[a] Department of Science Education and Application, National Taichung University of Education, Taichung 403, Taiwan
[b] College of Chemistry and Molecular Engineering, Peking University, Beijing 100871, China
[c] Department of General Education, National Taichung University of Science and Technology, Taichung 404, Taiwan

A R T I C L E   I N F O

A B S T R A C T

An ecofriendly and cheap photocatalyst is crucial for realizing practical photocatalysis applications. Many inorganic materials have modular structures in which individual units are responsible for different functions. [Bi$_2$O$_2$]$^{2+}$ slabs with an α-PbO-type structure and simple halide layers are effective spacers in some layered functional materials. Previous reports have mainly discussed electronic reasons for the different photocatalytic activities of layered PbBiO$_2$X-type materials (X = Cl, Br, I). To the best of our knowledge, nanocomposite semiconductors consisting of PbBiO$_2$I/g-C$_3$N$_4$ have not been reported in the literature. In this study, PbBiO$_2$X/g-C$_3$N$_4$ composites were isolated and characterized by FE-SEM-EDS, XRD, HR-XPS, TEM, PL, BET, FT-IR, and UV–vis-DRS. By degrading crystal violet (CV) and 2-hydroxybenzoic acid (HBA) in an aqueous solution under visible-light irradiation, the photocatalytic activities of PbBiO$_2$I/g-C$_3$N$_4$ are discussed further. In particular, the catalytic performance illustrates the best reaction rate constants of 0.3259 h^{-1} using the PbBiO$_2$I/g-C$_3$N$_4$ composite as the photocatalysts; these are 13.7 and 9.1 times higher than those of PbBiO$_2$I and g-C$_3$N$_4$, respectively. The quenching effects of different scavenger results demonstrate that reactive O$_2$$^{\cdot-}$ plays the major role and $\cdot$OH, h$^+$, and ^{1}O$_2$ play the minor role in CV degradation.

1. Introduction

Wastewater containing toxic chemicals can have harmful effects on living things and the environment. Therefore, the removal of such chemicals is the most important issue in modern pollution prevention technology. Countries are facing increasing environmental pollution and energy shortages. Therefore, photocatalytic technologies are playing an increasingly important role in pollutant removal and solar energy conversion [1]. Developing low-cost and ecofriendly photocatalysts is crucial for realizing practical applications [2].

Researchers have extensively studied layered Bi-based structural compounds that are part of the Aurivillius family, including BiOX (X = Cl, Br, I) [3,4], Bi$_4$Ti$_3$O$_{12}$ [5], and BiVO$_4$ [6], for application as strongly efficient photocatalysts. This is because these compounds show a unique layered structure and high catalytic activity. The levels of Bi 6 s and O 2p are believed to produce a predominantly dispersed hybrid valence band (VB) that promotes photogenerated hole mobility and oxidation reactions [7], thereby inducing photogenerated electron-hole pair segregation and subsequently increasing photocatalytic efficiency.

The structure of many inorganic materials is determined to be modular, with different functions being monitored by individual units. [Bi$_2$O$_2$]$^{2+}$ plates exhibiting an α-PbO type structure, in addition to having a simple halide layer, can form an effective spacer layer in some functional materials [8]. A study on the mechanism of different photocatalytic activities of layered lead bismuth oxyhalide (PbBiO$_2$X, X = Cl, Br, I)-type materials mainly discussed the electronic causes [9–17]. However, interpretation of the photocatalytic properties of the compounds should also take into account the arguments for crystal chemistry. The crystal structure and optical and redox properties of the oxides may together explain their different catalytic activities. The common property of all discussed solid materials is the crystallization in the layered structures. The materials possess halide-layer-separated covalent metal oxygen layers [PbBiO$_2$]$^+$ stacked along [001]. The crystal surface can be assumed to be comprising layers of metal oxygen; in other words, the (001) surfaces are expected to be formed by the metal atoms. Regarding bismuth compounds, it was statistically determined that lead and bismuth occupy the metal position in a ratio of 1:1 [18]. The PbBiO$_2$Cl [10,19], PbBiO$_2$Br [9,20], and PbBiO$_2$I [21]

---

band gap values have been reported to be 2.53, 2.47, and 2.39 eV, respectively. These values indicate that the gap determined for all of the aforementioned semiconductors is present in the visible region; therefore, they can be used for photocatalysis.

Studies have reported that heterojunctions associated with $PbBiO_2X$ (X = Cl, Br, I), including carbonized polymer dots (CPDs)/$PbBiO_2Br$ [22], $Ag/Ag_2O/PbBiO_2Br$ [23], $PbBiO_2Br/Cu_2O$ [24], $PbBiO_2Br/UiO$-66-NH_2 [25], $PbBiO_2Br/NbSe_2$ [26], $PbBiO_2Br/BiOBr$ [9], $PbBiO_2I/PbO$ [27], $PbBiO_2Cl/g$-C_3N_4 [28], $PbBiO_2Br/g$-C_3N_4 [29], $AgBr/Ag/PbBiO_2Br$ [30], $PbBiO_2I/Bi_5O_7I/g$-C_3N_4 [31], $PbBiO_2Br/PbO/g$-C_3N_4 [32], multi-walled carbon nanotube/$PbBiO_2Br$ [33], and $MoS_2/PbBiO_2I$ [34], show improved photocatalytic activity. In recent years, the heterojunction associated with $PbBiO_2X$ has attracted great interest owing to its suitable band gap, stability, and relatively excellent photocatalytic activity [9,11,25,27,29,30,34]. $PbBiO_2X$ composite has been found to exhibit higher photocatalytic activity than $PbBiO_2X$ in the photocatalytic degradation of organic compounds.

A review of relevant articles in the literature revealed that $PbBiO_2I/g$-C_3N_4 nanocomposite semiconductors have not been applied to photocatalysis. Therefore, this study sought to demonstrate the preparation of $PbBiO_2I/g$-C_3N_4 composites using a template-free hydrothermal method. In this study, the degradation of crystal violet (CV) and 2-hydroxybenzoic acid (HBA) was achieved in aqueous solution under visible light irradiation; the corresponding photocatalytic activity of the $PbBiO_2I/g$-C_3N_4 product produced was also investigated.

2. Experimental details

2.1. Materials

$Bi(NO_3)_3\cdot5H_2O$ (98 %, Sigma-Aldrich), $Pb(NO_3)_2\cdot H_2O$ (99 %, Katayama), crystal violet dye (CV; 99 %, Tokyo Kasei Kogyo Co.), 2-hydroxybenzoic acid (HBA; salicylic acid, 99 %, Katayama), *p*-benzoquinone (BQ, 98 %, Alfa Aesar), sodium azide (SA, 99.5 %, Sigma-Aldrich), isopropanol (IPA, 99.9 %, Merck), and ammonium oxalate (AO, 99 %, Osaka) were purchased according to the source and used in this study.

2.2. Analytical methods and instruments

Separation and identification procedures were performed using a liquid chromatography/mass spectrometry (LC/MS) apparatus (Waters ZQ), including an autosampler, binary pump, micromass detector, and photodiode array detector. High-performance LC/MS (HPLC-MS) was used to quantify the amount of residual dye in each reaction cycle [35]. In this study, field-emission transmission electron microscopy (FE-TEM) was performed using a microscope (JEOL-2010; 200 kV accelerating voltage), and regional electron diffraction, high-resolution TEM (HR-TEM), and energy-dispersive spectroscopy (EDS) were also performed. In addition, in this study, FE scanning electron microscopy (FE-SEM)-EDS was performed using a JEOL JSM-7401 F (acceleration voltage: 15 kV). The Micrometrics Gemini system was used to measure the Brunauer-Emmett-Teller (BET) specific surface area (S_{BET}) of the sample, where the adsorbate was nitrogen at the temperature of liquid nitrogen. X-ray diffraction (XRD) was performed using a MAC Science

MXP18 apparatus with Cu-Kα radiation and operating at 40 kV and 80 mA. In addition, Al-Kα radiation at 15 kV was applied. The ULVAC-PHI system was applied to perform HR X-ray photoelectron spectroscopy (HR-XPS).

2.3. Synthesis

2.3.1. $PbBiO_2I$

First, $Bi(NO_3)_3\cdot5H_2O$ (5 mmol) and $Pb(NO_3)_2\cdot H_2O$ (5 mmol) were mixed in a 50 mL flask, and then, 15 mL of 1 M HNO_3 was added. Next, 5 M NaOH was added dropwise, with continuous stirring to adjust the pH to 13; then, the pH was adjusted to 5. Subsequently, 5 mL of 1 M KI (5 mmol) was also added dropwise to form a white precipitate. Next, the solution was stirred vigorously for 30 min; 24 mL of the derivatized solution was transferred into an autoclave (30 mL) containing Teflon, and the autoclave was heated to 100–150 °C for 12 h and then cooled to room temperature. The resulting solid precipitate was collected by filtration. Next, the derivatized precipitate was washed with deionized water and ethanol to remove any possible ionic species, and then the precipitate was dried overnight at 60 °C. $PbBiO_2I$ (B5P5I5-13-200) can be achieved using the relevant $Pb(NO_3)_2/Bi(NO_3)_3/KI$ molar ratio (5:5:5), pH = 13, temperature (200 °C), and reaction time (12 h).

2.3.2. g-C_3N_4

The g-C_3N_4 powder was synthesized by calcining melamine directly in a muffle furnace under atmospheric conditions. The typical sequence in the synthesis is as follows. The first step is to place 5 g of melamine into a semi-closed alumina crucible that is also covered. The next step is to heat the crucible to 520 °C for 4 h (heating rate: 10 °C/min). After cooling the obtained product to room temperature, we obtained the g-C3N4 powder.

2.3.3. $PbBiO_2I/g$-C_3N_4

This process first requires mixing $PbBiO_2I$ (500–x mg) and g-C_3N_4 (x mg) in a 50-mL flask and then introducing ethylene glycol (10 mL). For the prepared samples, the sample codes ranged from B5P5I5-x%C3N4-13-100 (B5P5I5-x%-13-100) to B5P5I5-x%C3N4-13-150 (B5P5I5-x%-13-100; Table 1). The subsequent steps required vigorous stirring of the solution for 30 min; 30 mL of the solution was transferred to an autoclave (30 mL) containing Teflon, after which the autoclave was heated to 100–150 °C for 12 h and then naturally cooled to room temperature. A derivatized solid precipitate was obtained by filtration. Next, the derivatized precipitate was washed with deionized water and ethanol to remove any possible ionic species, and then, the precipitate was dried overnight at 60 °C.

2.4. Photocatalytic reactions

The stirred aqueous solution was transferred to a 100-mL flask for CV radiation experiments; a CV aqueous suspension (100 mL, 10 ppm) and a defined amount of catalyst powder were transferred to a Pyrex flask. The pH of the suspension was adjusted by adding NaOH or HNO_3 solution. To study the adsorption–desorption equilibrium of composites, we conducted experiments in the dark. The determined initial concentrations of the photocatalyst (10 mg) and CV aqueous solution

Table 1

Codes of as-prepared samples under different hydrothermal conditions.

Molar ratio(Bi:Pb:I) = 5:5:5				
pH value/ Temp (ºC)	g-C₃N₄ (weight%)			
	5	10	25	50	75
13-100	B5P5I5-5%-13-100	B5P5I5-10%-13-100	B5P5I5-25%-13-100	B5P5I5-50%-13-100	B5P5I5-75%-13-100
13-150	B5P5I5-5%-13-150	B5P5I5-10%-13-150	B5P5I5-25%-13-150	B5P5I5-50%-13-150	B5P5I5-75%-13-150

(100 mL) were mixed in a 100 mL flask; the resulting mixture was incubated at room temperature in an orbital shaker (100 rpm). Before irradiation, we maintained the temperature of the suspension at approximately 25 °C. Magnetic stirring was carried out for 30 min in the dark to achieve a balance of adsorption and desorption between the CV applied to the catalyst surface and the catalyst surface. Irradiation was performed using a Xe arc lamp (150 W) equipped with a 400-nm cut filter; the light intensity was set to 30.9 W/m^2, and the distance between the reaction vessel and the light source was set to 30 cm. A 5-mL aliquot was collected over the set irradiation time interval and centrifuged to remove the catalyst. HPLC-PDA-MS was used to quantify the amount of residual dye in each reaction cycle.

2.5. Quenching experiments

To measure the effects of active substances occurring during photocatalytic reactions, various quenchers were introduced to remove appropriate active substances. We examined ·OH, $O_2^{·−}$, h$^+$, and $^1O_2$, which are considered active species, by introducing the following: IPA (1.0 mM), an ·OH quencher [36]; BQ (1.0 mM), an $O_2^{·−}$ quencher [37]; AO (1.0 mM), an h$^+$ quencher [38]; and SA (1.0 mM), an $^1O_2$ quencher [39], respectively.

3. Results and discussion

3.1. Characterization of as-prepared samples

3.1.1. XRD

The pH of the hydrothermal reaction has been recognized as greatly affecting the composition and morphology of the product. Researchers have completed controlled experiments aimed at exploring the effects of pH on this reaction and reported that pH, in contrast to temperature and molar ratio, is indispensable in controlling crystal composition and anisotropic growth [35,40]. *t*-PbBiO$_2$I was derived at a pH of 13, with molar ratios (Bi:Pb:I) of 5:5:5 and reaction temperatures of 100 and 150 °C [31].

Figs. 1 and S1 show the XRD patterns of the prepared composites. Table 2 summarizes the XRD results obtained in this study. The pattern in Fig. 1 clearly indicates the presence of the following composites: *t*-PbBiO$_2$I/g-C$_3$N$_4$. The prepared sample contained *t*-PbBiO$_2$I (JCPDS 038-1007) and g-C$_3$N$_4$ (JCPDS 087-1526) phases. Table 2 summarizes the
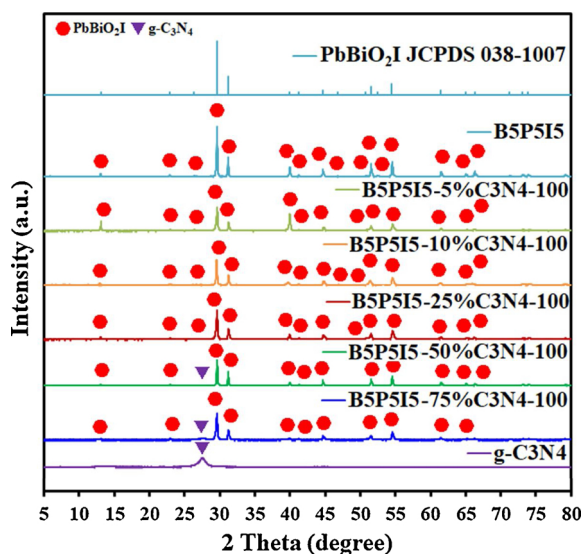

Fig. 1. XRD patterns of as-prepared samples under the conditions of pH of 13, reaction temperature of 100 °C, and reaction time of 12 h. (Molar ratio Pb (NO$_3$)$_2$/Bi(NO$_3$)$_3$ = 5/5 mmol/mmol, KI = 5 mmol).

Table 2
Crystalline phase changes of as-prepared samples under different bismuth oxyiodide weight of g-C$_3$N$_4$. (● PbBiO$_2$I ▲ g-C$_3$N$_4$).
● ▲

XRD results of other samples.

3.1.2. Morphological structure and composition

Two published articles have reported that the shape of PbBiO$_2$I may be square, irregular plates, or irregular long rods [14,27]. It is noted that the morphology of g-C$_3$N$_4$ is similar to that of irregular nano-sheets [41]. Fig. 2 shows a high-magnification PbBiO$_2$I, g-C$_3$N$_4$ and PbBiO$_2$I/ g-C$_3$N$_4$ FE-SEM image. It is noted that the morphology of the PbBiO$_2$I/ g-C$_3$N$_4$ composite sample is similar to that of the irregular plates, long rods, and irregular nano-sheets. The EDS results in Table 3 show that the derivative samples mainly consist of Pb, Bi, O, I, C, and N. The precursors were PbBiO$_2$I and g-C$_3$N$_4$; their calculated atomic ratios (%) were Pb: Bi: O: I = 1.00: 1.08: 4.07: 1.02 and C: N = 1.00: 1.27. These values were ascribed to PbBiO$_2$I and g-C$_3$N$_4$ phases. The stoichiometric ratios were Pb: Bi: I = 1: 1: 1 and C: N = 1: 1.33. These results indicate that the controlled hydrothermal method is effective for achieving selective composite synthesis.

3.1.3. TEM

Fig. 3 shows B5P5I5-25%C3N4-13-100-12 (*t*-PbBiO$_2$I/g-C$_3$N$_4$) consisting of long rods, irregular plates, and irregular nano-sheets, which exhibit different sizes. The EDS spectrum indicates that Pb, Bi, I, O, C, and N were also determined to be components of the derived sample. As shown in the HR-TEM image in Fig. 3(d), this study yielded two sets of lattice images that revealed d-spacing values of 0.218 and 0.177 nm, respectively, owing to the (114) and (116) planes of *t*-PbBiO$_2$I; in this study, this observation is in good agreement with the XRD results. The results show that the phase structure of *t*-PbBiO$_2$I/g-C$_3$N$_4$ in the derivatized complex is beneficial to photoinduced carrier segregation and produces high levels of photocatalytic activity.

3.1.4. XPS

Fig. 4 shows the Pb 4f, Bi 4f, O 1s, I 3d, C 1s, and N 1s XPS spectra of the *t*-PbBiO$_2$I /g-C$_3$N$_4$ composite. The transition peak is related to the orbit of Bi 4f, Pb 4f, O 1s, I 3d, C 1s, and N 1s that represent Bi, Pb, O, I, C and N, the constituents of the derivatized catalyst. Fig. 4(b) shows the spectrum of the Pb 4f deconvoluted as a peak at the binding energy of 137.2 eV owing to Pb 4f$_{7/2}$, which may be due to the presence of Pb in the divalent oxidation state [31]. Chen et al. determined that the particle size of PbBiO$_2$Cl may be related to the significant change in the binding energy of the Pb peak [11]. Fig. 4(c) reveals a spectrum obtained by the binding energy of Bi 4f at 158.3 eV owing to the two peaks of Bi 4f$_{7/2}$, which are also determined to be Bi in the trivalent oxidation state. The Bi^{3+} phase in the *t*-PbBiO$_2$I/g-C$_3$N$_4$ composite can explain these 4f$_{7/2}$ peaks.

Chen et al. [42] also made comparable chemical binding observations for Bi 4f$_{7/2}$. In addition, the asymmetric peaks derived from the O 1s spectrum shown in Fig. 4(d) can be convoluted using the XPS peak fitting procedure, and the O 1s peaks are generated at 528.9 eV, which are determined to be in the oxygen atom of the *t*-PbBiO$_2$I lattice [35]. The secondary peak (530.8 eV) can be assigned to the hydroxyl groups on the surface. As shown in Fig. 4(e), it was determined that the peak observed at the binding energy of 618.3 eV corresponds to I 3d$_{5/2}$ owing to the I present in the monovalent oxidation state of *t*-PbBiO$_2$I. Fig. 4(f) shows the C 1s spectrum of the composite; it mainly shows two carbon atoms, sp^2 C−C bond (284.3 eV) and sp2-hybrid carbon, that are determined to be present in the N-containing aromatic ring (N−C═N, 287.8 eV). A study demonstrated the latter to be the primary species in polymeric g-C$_3$N$_4$ [43]. As shown in Fig. 4(g), the spectrum of N 1s can be deconvolved into three peaks: 398.3, 399.1, and 400.1 eV. It was
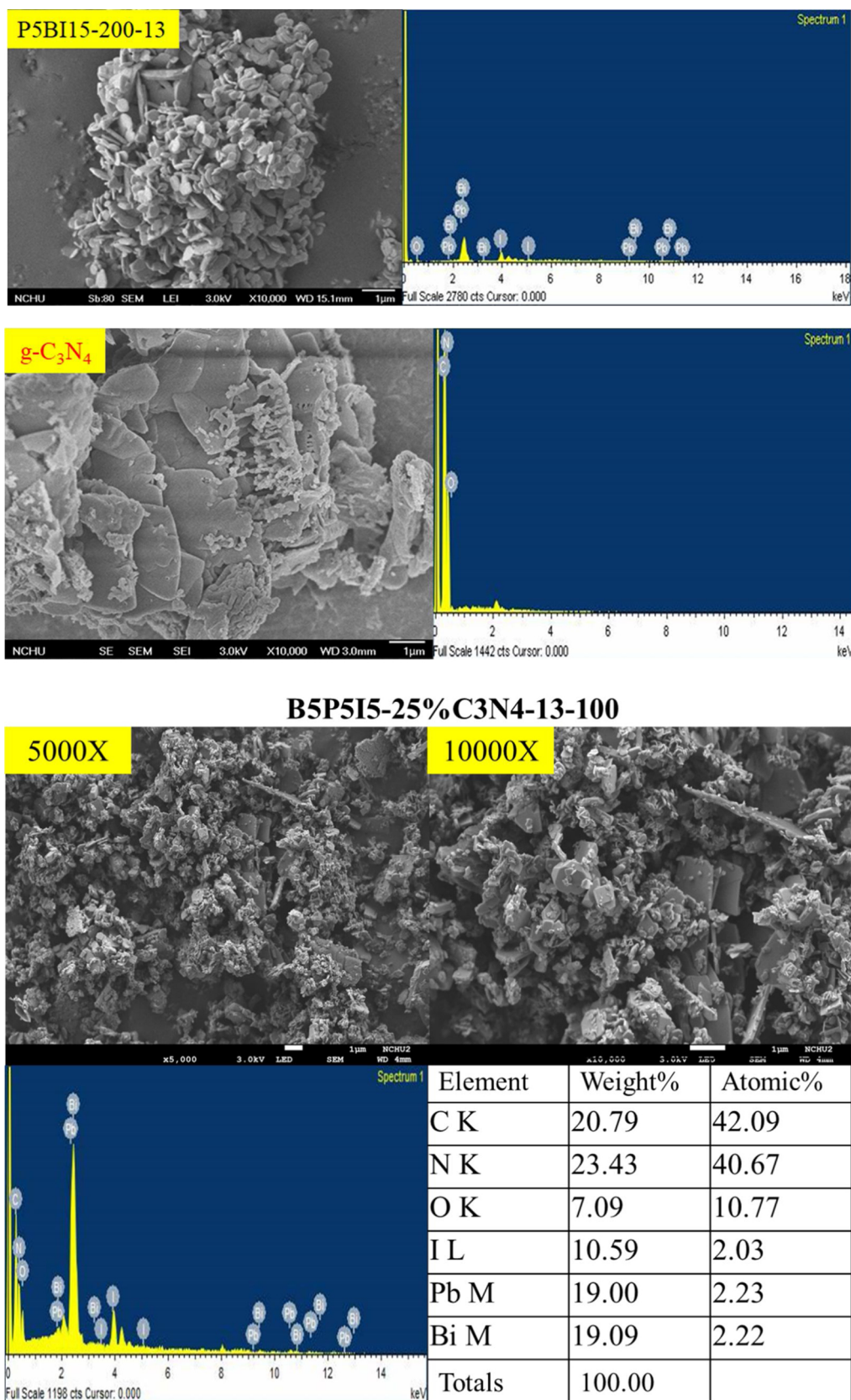
Fig. 2. SEM images and EDS of PbBiO$_2$I, g-C$_3$N$_4$, and B5P5I5-25%C3N4-13-100-12 (PbBiO$_2$I/g-C$_3$N$_4$) yielded by the hydrothermal autoclave method.

determined that the highest peak centered at 398.3 eV corresponds to the sp^2-hybrid nitrogen contained in the triazine ring (C−N=C), and it should be noted that the peak recorded at 399.1 eV corresponds to the tertiary N−(C)$_3$ groups. Except for sp^2-hybridized carbon (N−C=N, 287.8 eV), both units were identified as units constituting the heptazine heterocycle, thereby forming the basic unit of the substructure of the g-
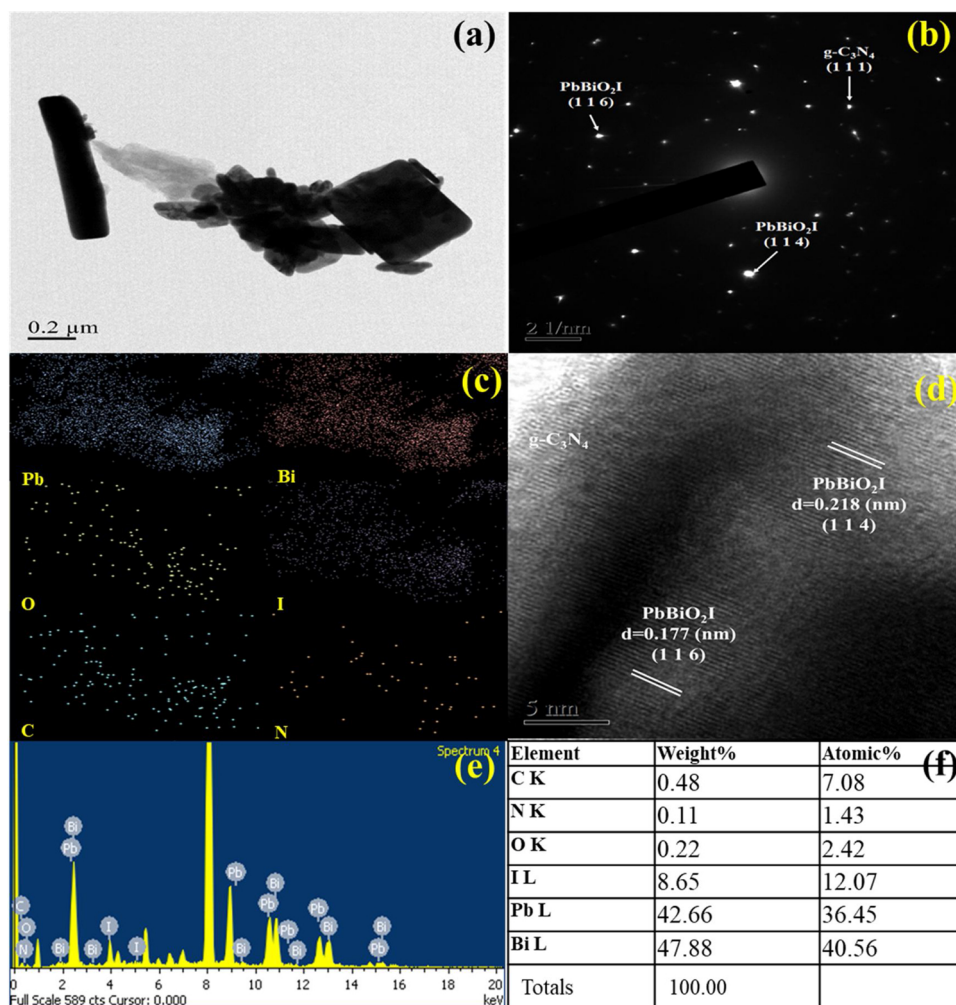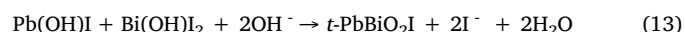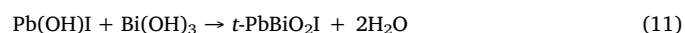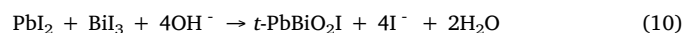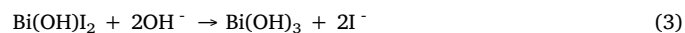
Table 3

EDS of the as-prepared $PbBiO_2I$ materials obtained using different $g-C_3N_4$ contents at reaction temperatures of 100 and 150 °C and reaction time of 12 h.

Sample code	Atomic ratio (%)					
	Pb	Bi	O	I	C	N
B5P5I5-13-200	14.92	16.60	54.05	14.43	–	–
B5P5I5-5%-13-100	1.67	2.18	13.34	1.79	47.6	33.42
B5P5I5-10wt%-100	1.04	1.21	11.65	1.31	47.92	36.88
B5P5I5-25wt%-100	2.23	2.22	10.77	2.03	42.09	40.67
B5P5I5-50wt%-100	1.68	1.97	12.10	1.49	52.36	30.40
B5P5I5-75wt%-100	0.98	1.20	7.37	1.03	45.95	43.47
B5P5I5-5%-150	5.92	6.53	13.09	6.35	41.74	26.36
B5P5I5-10wt%-150	2.64	2.92	15.08	2.79	46.85	29.71
B5P5I5-25wt%-150	5.78	6.24	20.66	5.63	38.49	23.20
B5P5I5-50wt%-150	3.31	3.52	16.19	1.90	49.48	25.59
B5P5I5-75wt%-150	1.98	2.30	17.03	1.93	58.31	18.44
$g-C_3N_4$	0	0	0	0	44.05	55.95

C_3N_4 polymer. Finally, it was determined that the weak peak observed at 400.1 eV corresponds to the charge effect or positive charge localization of the heterocycle [44]. The proposed results are consistent with the XRD and TEM results.

Chen et al. [11,42,45] demonstrated the formation process associated with a range of bismuth oxybromides and lead bismuth oxychloride. Eqs. (1–17) describe the formation of t-$PbBiO_2I$ proposed in the current study. The compounds that were realized under various hydrothermal conditions were demonstrated to undergo a series of changes, as shown in Fig. 5. The pH values of the hydrothermal reactions were controlled to obtain various compositions:

$$Bi^{3+} + 3I^- \rightarrow BiI_3 \tag{1}$$

$$BiI_3 + OH^- \rightarrow Bi(OH)I_2 + I^- \tag{2}$$

$$Bi(OH)I_2 + 2OH^- \rightarrow Bi(OH)_3 + 2I^- \tag{3}$$

$$Pb^{2+} + 2I^- \rightarrow PbI_2 \tag{4}$$

$$PbI_2 + OH^- \rightarrow Pb(OH)I \tag{5}$$

$$Pb(OH)I_{(s)} + OH^- \rightarrow Pb(OH)_2 + I^- \tag{6}$$

$$PbI_2 + Bi(OH)_3 + OH^- \rightarrow t\text{-}PbBiO_2I + I^- + 2H_2O \tag{7}$$

$$PbI_2 + Bi(OH)_2I + 2OH^- \rightarrow t\text{-}PbBiO_2I + 2I^- + 2H_2O \tag{8}$$

$$PbI_2 + Bi(OH)I_2 + 3OH^- \rightarrow t\text{-}PbBiO_2I + 3I^- + 2H_2O \tag{9}$$

$$PbI_2 + BiI_3 + 4OH^- \rightarrow t\text{-}PbBiO_2I + 4I^- + 2H_2O \tag{10}$$

$$Pb(OH)I + Bi(OH)_3 \rightarrow t\text{-}PbBiO_2I + 2H_2O \tag{11}$$

$$Pb(OH)I + Bi(OH)_2I + OH^- \rightarrow t\text{-}PbBiO_2I + I^- + 2H_2O \tag{12}$$

$$Pb(OH)I + Bi(OH)I_2 + 2OH^- \rightarrow t\text{-}PbBiO_2I + 2I^- + 2H_2O \tag{13}$$

$$Pb(OH)I + BiI_3 + 3OH^- \rightarrow t\text{-}PbBiO_2I + 3I^- + 2H_2O \tag{14}$$

Element	Weight%	Atomic%
C K	0.48	7.08
N K	0.11	1.43
O K	0.22	2.42
I L	8.65	12.07
Pb L	42.66	36.45
Bi L	47.88	40.56
Totals	100.00	

Fig. 3. (a) FE-TEM images, (b) SAD, (c) mapping, (d) HR-image, and (e), (f) EDS of $PbBiO_2I/g-C_3N_4$ (B5P5I5-25%C3N4-13-100-12) samples yielded by the hydrothermal autoclave method.
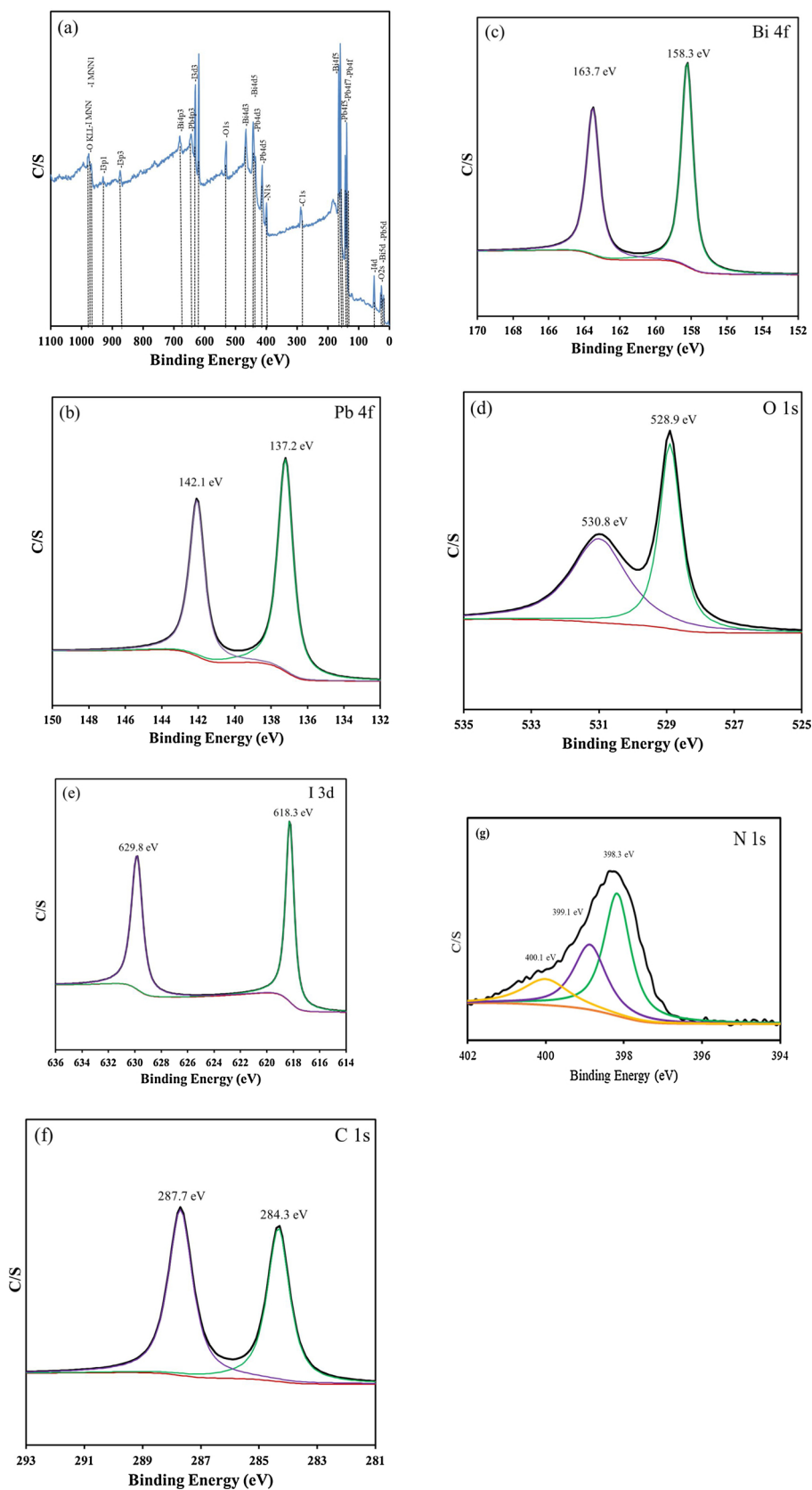
Fig. 4. XPS spectra of as-prepared samples under different pH values at reaction temperature of 100 °C and reaction time of 12 h. (Molar ratio $Pb(NO_3)_2/Bi(NO_3)_3 =$ 5/5 mmol/mmol, KI = 5mmol). (a) Total survey, (b) Pb 4f, (c) Bi 4f, (d) O 1s, (e) I 3d, (f) C 1s, and (g) N 1s.
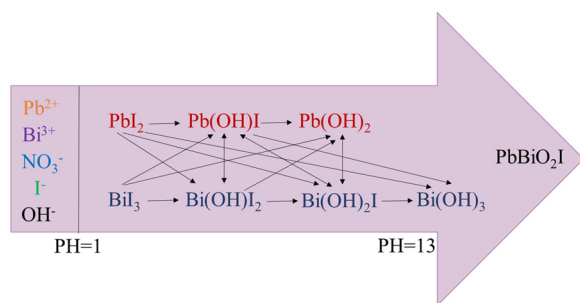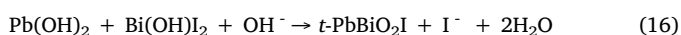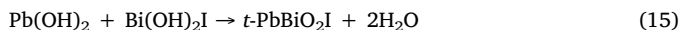
Fig. 5. *t*-PbBiO$_2$I formation processes proposed by controlling the hydrothermal reaction's pH value.

$$Pb(OH)_2 + Bi(OH)_2I \rightarrow t\text{-}PbBiO_2I + 2H_2O \tag{15}$$

$$Pb(OH)_2 + Bi(OH)I_2 + OH^- \rightarrow t\text{-}PbBiO_2I + I^- + 2H_2O \tag{16}$$

$$Pb(OH)_2 + BiI_3 + 2OH^- \rightarrow t\text{-}PbBiO_2I + 2I^- + 2H_2O \tag{17}$$

3.1.5. Fourier-transform infrared spectroscopy

Fig. S1 of Supporting information shows the Fourier-transform infrared spectrum of the *t*-PbBiO$_2$I/g-C$_3$N$_4$ composite (achieved at different weight percentages), showing strong absorption mainly at 400–900 cm^{-1}; it is noted that this corresponds to Pb−O, Bi-O, Bi-O-Bi, and Bi-O-I in the stretching vibration of *t*-PbBiO$_2$I [46]. Regarding pure g-C$_3$N$_4$, peaks were observed at 1253, 1329, 1420, 1571, and 1646 cm^{-1}, which this study found were corresponding to the typical stretching mode corresponding to the CN heterocycle [41]. In addition, the results show that the typical breathing pattern of the triazine unit is at 812 cm^{-1} [47], which is consistent with the XRD and TEM results. Furthermore, ν(C−O) stretching vibrations were noted to be represented by a strong broad band that was located at 1388 cm^{-1}. The (O−C−O) out-of-plane vibration was represented by a medium strong band that was located at ∼821 cm^{-1}. As indicated by the infrared spectrum of PbCO$_3$·xH$_2$O (or Bi(CO$_3$)$_3$·xH$_2$O), some of the derivatives in this study have water molecules that are not coordinated. As expected, the ν(O−H) stretching vibration correlation band associated with the uncoordinated H$_2$O was found to be present at ∼3100 cm^{-1}. However, as indicated in Fig. 4(b), the spectra derived for Pb 4f$_{7/2}$ were not deconvoluted in this study into two peaks at 137.2-eV binding energy that was attributable to *t*-PbBiO$_2$I but not to PbCO$_3$; it could be caused by Pb existing in the divalent oxidation state, and PbCO$_3$ only produces a catalyst surface with very little content. The results presented are consistent with the XPS results.

3.1.6. Optical absorption properties

For the prepared sample, the diffuse reflectance UV–vis spectrum (DR-UV–vis) spectroscopy results show that the absorption edge of the sample is approximately 470–590 nm (Fig. 6), which is the band gap of 2.25–2.54 eV and is consistent with the reported results [21,48,49]. Pure *t*-PbBiO$_2$I and g-C$_3$N$_4$ only absorb an appropriate amount of visible light. An $(\alpha h\nu)^{1/2}$ plot against energy $(h\nu)$ was used to determine the *t*-PbBiO$_2$I/g-C$_3$N$_4$ E_g value (i.e., 2.25 eV). The figure shows that the *t*-PbBiO$_2$I/g-C$_3$N$_4$ composite with different g-C$_3$N$_4$ contents showed effective light absorption for wavelengths exceeding 551.1 nm, demonstrating that the *t*-PbBiO$_2$I/g-C$_3$N$_4$ composites are effective visible-light-driven photocatalysts. Moreover, the absorption intensity of the *t*-PbBiO$_2$I/g-C$_3$N$_4$ composites in the entire spectrum is obviously enhanced, and the absorption edge of the *t*-PbBiO$_2$I/g-C$_3$N$_4$ composites is significantly red-shifted compared with that of the pure g-C$_3$N$_4$. The pure g-C$_3$N$_4$ particles are light-yellow powders. With the introduction of *t*-PbBiO$_2$I, the *t*-PbBiO$_2$I/g-C$_3$N$_4$ composite gradually turns into a yellow-brown powder, thereby exhibiting enhanced visible light absorption. Fig. 6 (inset) shows the conventional Tauc plot of crystalline *t*-
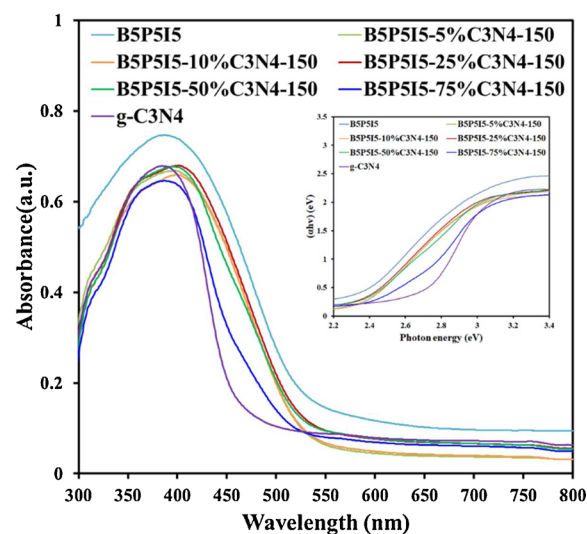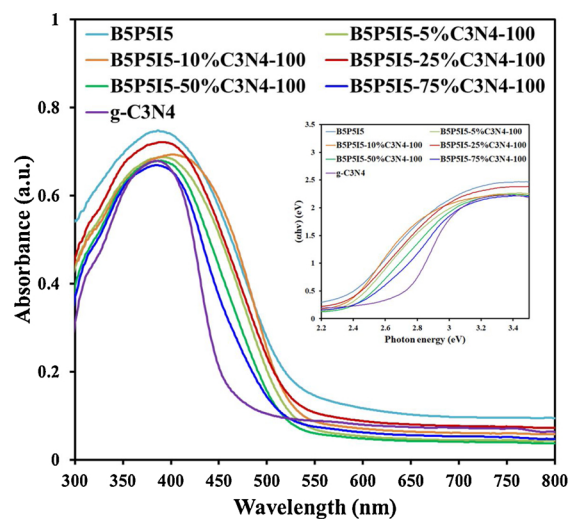

Fig. 6. UV–vis absorption spectra of the as-prepared photocatalysts.

Table 4
Physical and chemical properties of as-prepared samples under different conditions (Pb(NO$_3$)$_2$/Bi(NO$_3$)$_2$ = 5/5 mmol/mmol, KI = 5 mmol, pH = 13, temp = 100 °C, time = 12 h.

Samples	S$_{BET}$ (m^2 g^{-1})	Pore volume (cm^3 g^{-1})	Pore diameter (nm)	Band gap (eV)
B5P5I5	13.4705	0.165003	496.773	2.29
B5P5I5-25%C3N4-13-100	17.1418	0.186470	348.210	2.25
g-C$_3$N$_4$	18.4363	0.176410	318.347	2.68

PbBiO$_2$I, g-C$_3$N$_4$, and *t*-PbBiO$_2$I/g-C$_3$N$_4$; the bandgap (2.29 and 2.68 eV) of *t*-PbBiO$_2$I and g-C$_3$N$_4$ (Table 4) could be easily obtained by extrapolating to the x-axis. The introduction of g-C$_3$N$_4$ enhances the ability of *t*-PbBiO$_2$I to respond to more visible light to generate more photogenerated carriers and enhance their photocatalytic performance.

3.1.7. Nitrogen adsorption–desorption isotherm

Fig. 7 illustrates the nitrogen adsorption–desorption isotherms derived from *t*-PbBiO$_2$I/g-C$_3$N$_4$, *t*-PbBiO$_2$I, and g-C$_3$N$_4$. Note that the *t*-PbBiO$_2$I/g-C$_3$N$_4$ isotherm is close to the type IV isotherm, and a
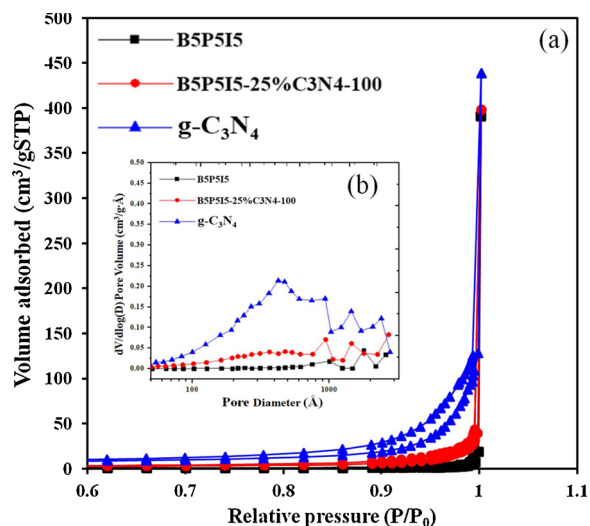
Fig. 7. (a) Nitrogen adsorption–desorption isotherms and (b) corresponding pore size distribution curve (inset) for B5P5I5-25%C3N4-13-100.

hysteresis loop is observed at a relatively high pressure of 0.6–1.0 [50]. Because such types of self-organized porous architectures afford highly efficient pathways for reactant and product molecule transport, they have been determined to be remarkably valuable in photocatalysis [51]. From Table 4, the t-PbBiO$_2$I, g-C$_3$N$_4$, and t-PbBiO$_2$I/g-C$_3$N$_4$ samples had S_{BET} values of 13.5, 18.4, and 17.1 m^2/g, respectively. The pore volume and diameter of t-PbBiO$_2$I/g-C$_3$N$_4$ were 0.19 cm^3/g and 348 nm, respectively.

Table 5
Pseudo first-order rate constant for CV photocatalytic oxidation using diff ;erent photocatalysts.

Photocatalyst	k (h^{-1})	R^2
B5P5I5	0.0358	0.9893
B5P5I5-5%C3N4-100	0.0269	0.7895
B5P5I5-10%C3N4-100	0.0759	0.9947
B5P5I5-25%C3N4-100	0.3259	0.9122
B5P5I5-50%C3N4-100	0.1716	0.9987
B5P5I5-75%C3N4-100	0.0609	0.9958
B5P5I5-5%C3N4-150	0.2367	0.9899
B5P5I5-10%C3N4-150	0.2515	0.9497
B5P5I5-25%C3N4-150	0.2702	0.9307
B5P5I5-50%C3N4-150	0.0619	0.9836
B5P5I5-75%C3N4-150	0.0301	0.9574
g-C$_3$N$_4$	0.0238	0.9876

3.2. Photocatalytic activity

Fig. 8(a), (b) show the UV–vis spectra of the aqueous dispersion of t-PbBiO$_2$I/g-C$_3$N$_4$ during the photodegradation of CV and HBA under visible-light irradiation. The experimental results showed that approximately 99.5 % of the CV degraded after 12 h of irradiation as described above, and approximately 72 % of the HBA degraded after 72 h. Fig. 8(c), (d) shows the degradation efficiency as a function of the reaction time. The removal efficiency can be improved significantly by using the prepared sample. In the absence of a photocatalyst, the CV does not degrade under visible-light illumination. After irradiation for 12 h, the photocatalytic performance of t-PbBiO$_2$I/g-C$_3$N$_4$ exceeded that of other samples, and the removal efficiency of CV dye was as high as 99.5 %. To obtain a clearer understanding of the kinetics of CV dye
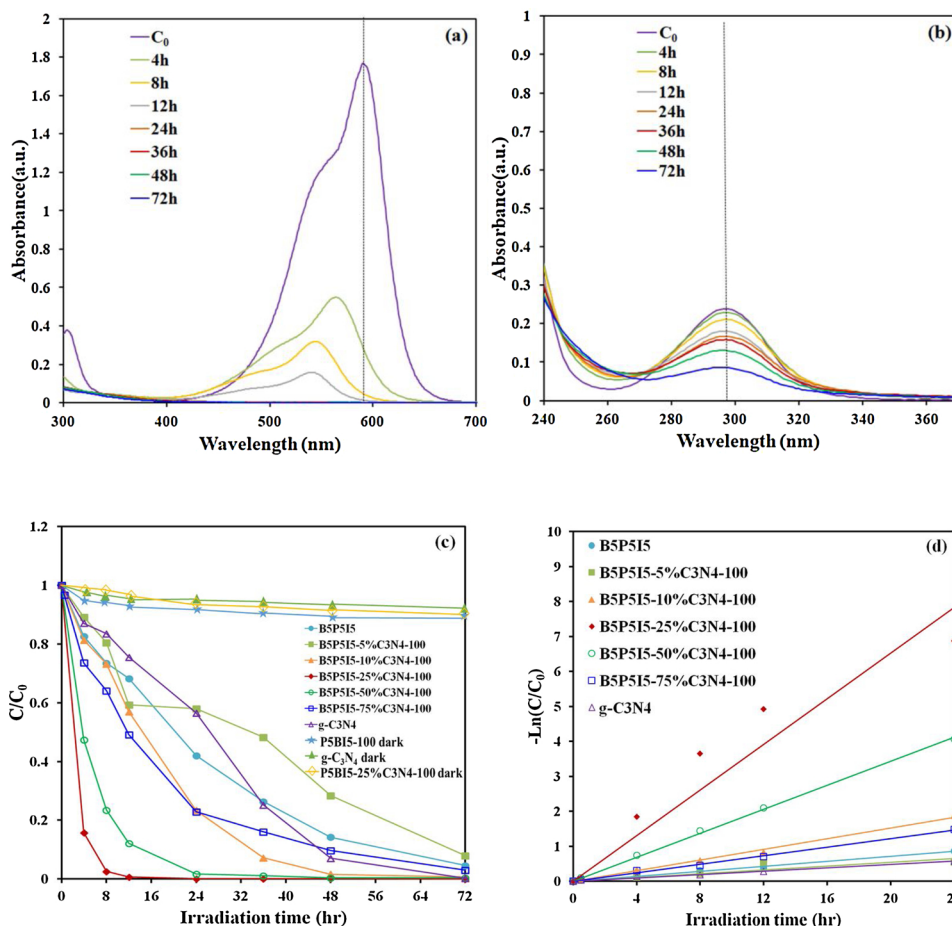

Fig. 8. Temporal UV–vis adsorption spectral changes during the photocatalytic degradation of (a) CV and (b) HBA over aqueous PbBiO$_2$I/g-C$_3$N$_4$ under visible-light irradiation. (c), (d) Photocatalytic activity of as-prepared samples for CV photocatalytic degradation under different amounts of g-C$_3$N$_4$. (Molar ratio Pb(NO$_3$)$_2$/Bi(NO$_3$)$_3$ = 5/5 mmol/mmol, KI = 5 mmol, reaction temperature = 100 °C, pH = 13, reaction time = 12 h.)

degradation, this study performed an apparent pseudo first-order model [52]; that is, $\ln(Co/C) = kt$. The data shown in Table 5 were subjected to a first-order linear fit; therefore, the k value of t-PbBiO$_2$I/g-C$_3$N$_4$ (B5P5I5-5-75% C3N4-100) was derived to $3.259 \times 10^{-1} h^{-1}$ (maximum degradation rate). Its derivation value greatly exceeds other composite materials; compared with other composite materials, the t-PbBiO$_2$I/g-C$_3$N$_4$ (B5P5I5-5-75%C3N4-100) photocatalyst found in this study has significantly higher efficiency. The t-PbBiO$_2$I/g-C$_3$N$_4$ (B5P5I5-5-75%C3N4-100) composite has excellent photocatalytic activity, which may be attributed to its efficient use of visible light and high separation efficiency of electron–hole pairs having a layered structure. The B5P5I5-25%C3N4-100 (t-PbBiO$_2$I/g-C$_3$N$_4$) composite with a large S_{BET} exhibited the highest photocatalytic ability among all the samples, suggesting that changes in the photocatalytic ability were associated with the BET surface area, its efficient use of visible light, and the highly effective separation of electron–hole pairs within its samples. To evaluate the durability of the B5P5I5-25%C3N4-100 (t-PbBiO$_2$I/g-C$_3$N$_4$) composite, this study recovered the previously used catalyst. The catalyst was collected after each cycle by centrifugation. After the removal of CV in the fourth cycle, no significant defects in photocatalytic activity were observed, and the defect determined during the fifth run was 3.6 % [Fig. 9(a)]. After probing the previously used t-PbBiO$_2$I/g-C$_3$N$_4$ by XRD, the study determined that there was no difference between the previously used sample and the prepared sample (Fig. 9(b)); therefore, the obtained t-PbBiO$_2$I/g-C$_3$N$_4$ composite has good stability under light irradiation.

To explore the recombination rate of photogenerated electron–hole pairs, the current research used photoluminescence (PL) spectroscopy. In addition, to investigate the segregation ability of photo-generated carriers in heterostructures, this study used the t-PbBiO$_2$I/g-C$_3$N$_4$ PL spectrum (Fig. 10). The results showed a strong g-C$_3$N$_4$ emission peak at ~462 nm; it is caused by the direct electron–hole recombination of the energy band transition. Nevertheless, the innate emission peak observed for t-PbBiO$_2$I was approximately 462 nm (lowest intensity). The obtained results indicate the significant inhibition of photogenerated carrier recombination. Effective charge isolation can result in an increase in the charge carrier lifetime and in the efficiency of interface charge transfer to the adsorbed substrate, resulting in enhanced photocatalytic activity. The observed photocatalytic activity of the t-PbBiO$_2$I/g-C$_3$N$_4$ heterojunction reached $0.3259 h^{-1}$ (maximum rate constant); it exceeded the estimated values of the t-PbBiO$_2$I and g-C$_3$N$_4$ photocatalysts by 9.1 and 13.7 times, respectively. Therefore, the results show that the t-PbBiO$_2$I/g-C$_3$N$_4$ heterojunction is indispensable in the enhancement of photocatalytic activity. Therefore, the previous PL results obtained in this study confirmed the importance of the composite in suppressing electron–hole recombination and explained the enhanced photocatalytic performance of the t-PbBiO$_2$I/g-C$_3$N$_4$ composite.

3.3. CV photodegradation mechanism

To evaluate the effect of the active substance in the photocatalytic reaction, various quenchers were introduced to remove suitable active substances [53]. The introduction of BQ, IPA, AO, and SA quenchers reduced the photocatalytic degradation of CV dyes compared to the case in which no quencher was introduced [Fig. 11(a)], thus indicating that $O_2^{\cdot-}$ is the main active substance and that $^{\cdot}OH$, h^+, and $^1O_2$ act as secondary active substances in the CV photocatalytic degradation mechanism.

As illustrated in Fig. 11(b) and (c), when the reaction was executed in the dark, no EPR signals were observed. However, when the reaction process was conducted under visible light, intensity signals corresponding to the characteristic peak of DMPO-O$_2^{\cdot-}$ adducts (Fig. 11(b)) were noted; trials with lengthened reaction times resulted in gradual increases in the intensity. However, when the reaction process was conducted under visible light, DMPO-$^{\cdot}OH$ adducts (Fig. 11(c)) were not noted, and trials with lengthened reaction times resulted in gradual
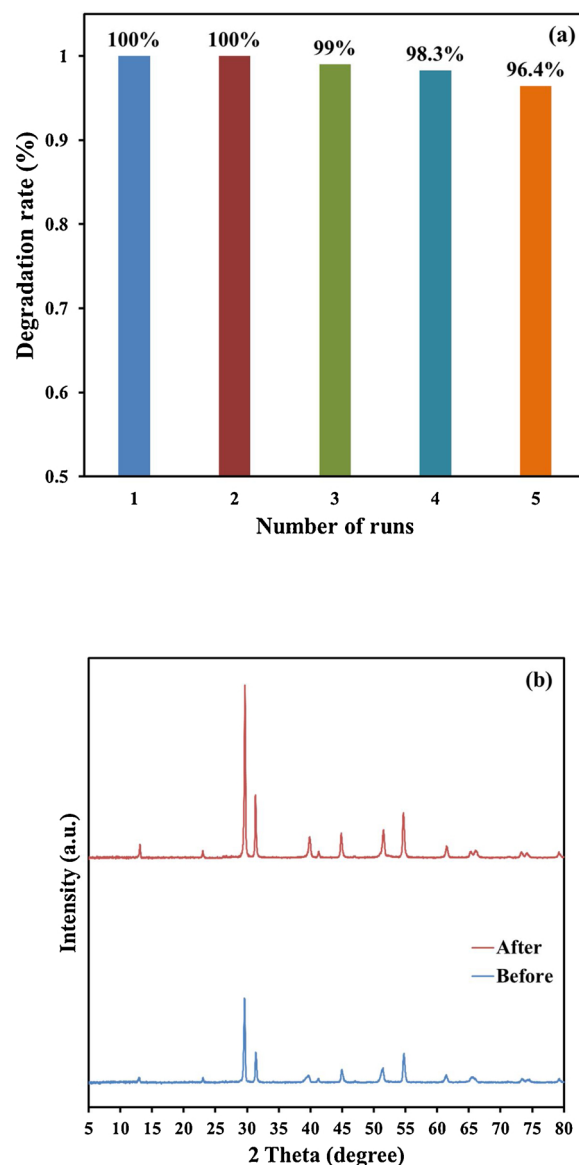
Fig. 9. (a) Cycling runs and (b) XRD patterns acquired before and after photocatalytic degradation of CV in the presence of B5P5I5-13-100-25 wt% (PbBiO$_2$I/g-C$_3$N$_4$).

reductions in the intensity. This suggests that the $O_2^{\cdot-}$ and $^{\cdot}OH$ active species were formed in the presence of PbBiO$_2$I/g-C$_3$N$_4$ composite and oxygen under the irradiation provided by visible light.

The results obtained from the structural characterization performed showed that the t-PbBiO$_2$I/g-C$_3$N$_4$ photocatalyst was a two-phase composite. The photocatalytic activity of the resulting composite greatly exceeded the activity of the separately determined component phase. Therefore, it is assumed that there may be a synergy between t-PbBiO$_2$I and g-C$_3$N$_4$. In fact, many researchers have shown that there are synergistic effects in composites containing two contacted semiconductors [54,55], where the effects mentioned are due to the efficient charge transfer achieved at the interface of the two semiconductors. This phenomenon may increase the photo-hole segregation effect of photoexcitation, thereby enhancing the photocatalytic activity. The charge transfer process is affected by the energy potential. Therefore, a suitable band potential constitutes a prerequisite associated with the synergy of the composite photocatalyst. Fig. 12 shows the energy band derivation derived from the type II heterostructure [56] and the VB XPS spectra derived from t-PbBiO$_2$I and g-C$_3$N$_4$. It is noted that the CB and
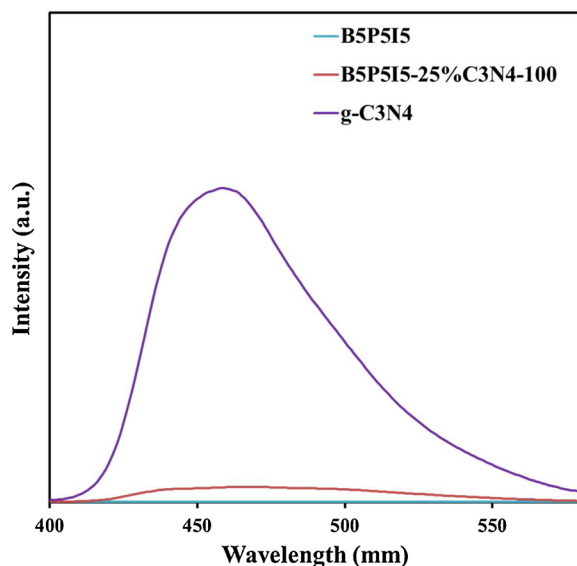
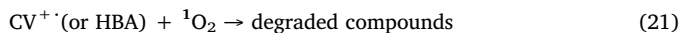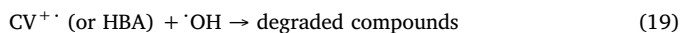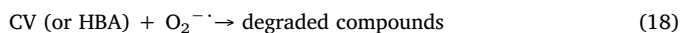**Fig. 10.** PL spectra of the as-prepared photocatalysts under different pH values and reaction temperature. (Molar ratio $Pb(NO_3)_2/Bi(NO_3)_3 = 5/5$ mmol/mmol, KI $= 5$ mmol, hydrothermal conditions: pH $= 13$, temperature $= 100$ °C, reaction time $= 12$ h).

VB positions observed in the g-C_3N_4 semiconductor are higher than those determined in the t-$PbBiO_2I$ semiconductor, and the step directions of CB and VB are the same (Fig. 12). The VB edge of g-C_3N_4 is approximately 1.58 eV, which is consistent with the position indicated by Li et al. [56]. Regarding t-$PbBiO_2I$, the derived VB edge is 1.83 eV. Therefore, it is proved that the band potential derived from t-$PbBiO_2I$ and g-C_3N_4 is suitable. The photogenerated electrons present on the surface of the g-C_3N_4 sample can be conveniently transferred to t-$PbBiO_2I$, both of which occur through the interface. Similarly, the holes present on the surface of the t-$PbBiO_2I$ sample can migrate to g-C_3N_4. Therefore, the observed charge transfer effectively prevents electron–-hole recombination in the two semiconductors, thereby promoting an increase in photocatalytic efficiency.

Fig. 12 shows the dye degradation mechanism based on the experimental results described in the previous paragraph. When the electron reaches the conduction band of t-$PbBiO_2I/g$-C_3N_4, it immediately promotes the production of reactive oxygen species, leading to the degradation of the CV dye. Obviously, in addition to the CV dye photodegradation executed through the routes of t-$PbBiO_2I/g$-C_3N_4-mediated and -photosensitized processes, another route explains the photocatalytic activity augmentation. Both photosensitized and photocatalytic processes are performed simultaneously (Fig. 12). However, under the conditions associated with photosensitized and photocatalytic reactions, photogenerated and photosensitized electrons react with the oxygen present on the surface of the photocatalyst to produce $O_2{}^{\cdot-}$ free radicals; further, the $O_2{}^{\cdot-}$ radical reacts with H^+ and H_2O to form an $^{\cdot}OH$ radical and H_2O_2, and the $O_2{}^{\cdot-}$ radical reacts with h^+ to form $^1O_2$. These cycles are maintained when visible light is irradiated on the system [57]; once many photooxidation cycles are exhausted, Eqs. (18–21) can describe the degradation of the CV dye (or HBA) caused by the oxidant produced.

$$CV \text{ (or HBA)} + O_2{}^{-\cdot} \rightarrow \text{degraded compounds} \qquad (18)$$

$$CV^{+\cdot} \text{ (or HBA)} + {}^{\cdot}OH \rightarrow \text{degraded compounds} \qquad (19)$$

$$CV \text{ (or HBA)} + h^+ \rightarrow \text{degraded compounds} \qquad (20)$$

$$CV^{+\cdot} \text{(or HBA)} + {}^1O_2 \rightarrow \text{degraded compounds} \qquad (21)$$

Studies have shown that hydroxylated compounds can degrade photocatalytic CV dyes in visible-light-galvanized semiconductor
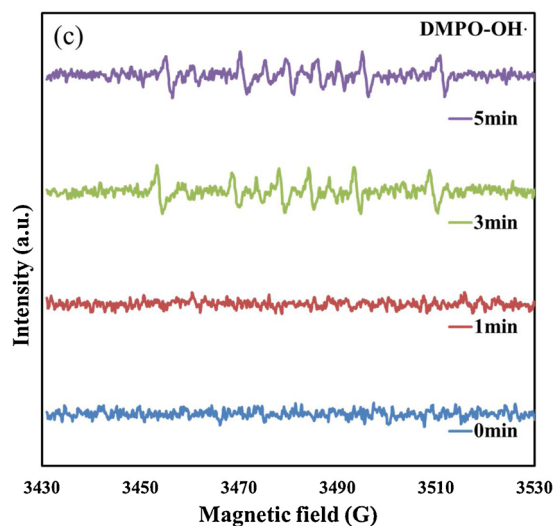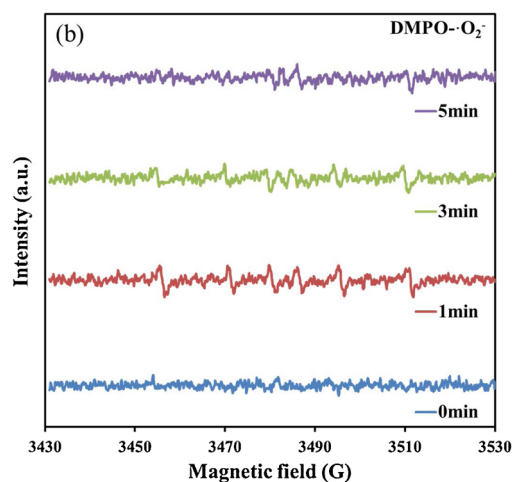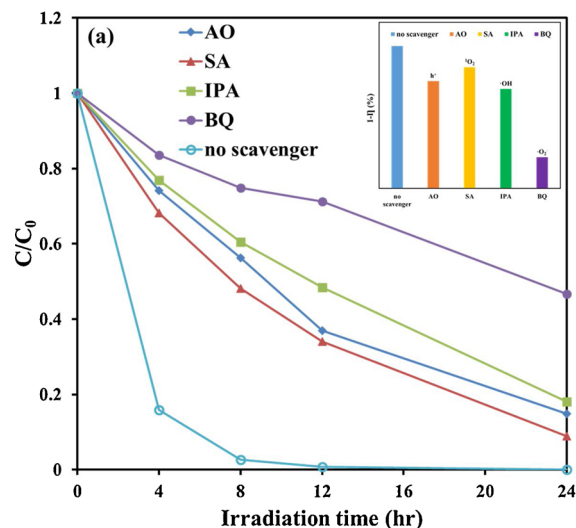

Fig. 11. (a) Photodegradation of CV dye (P5B3-10-100-15 wt%) in the presence of different scavengers under solar light irradiation. DMPO spin-trapping EPR spectra of (b) DMPO $-^{\cdot}O_2{}^-$ and (c) DMPO-$^{\cdot}OH$ under visible-light irradiation with B5P5I5-25 wt%C3N4-13-100.
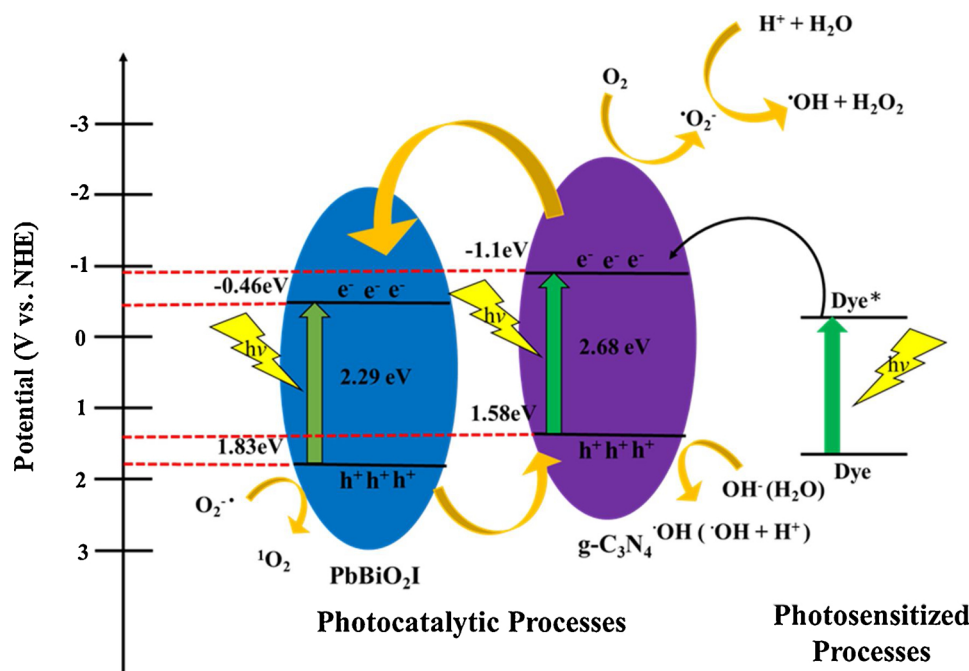
Fig. 12. Schematic of the band gap structures of B5P5I5-25 wt%-13-100 ($PbBiO_2I/g\text{-}C_3N_4$).

systems [57]. Previous reports [35,40,50] have demonstrated that in the photocatalytic degradation of CV dyes under UV or visible-light irradiation, nitrogen-centered free radical generation precedes *N*-dealkylation and carbon-centered free radical formation precedes the decomposition of the dye chromophore structure. The derivatization mechanism of the proposed photocatalytic method of *t*-$PbBiO_2I/g\text{-}C_3N_4$ loading can be used as a reference for applications related to dye decolorization.

4. Conclusions

In this study, a template-free hydrothermal method was implemented to synthesize the *t*-$PbBiO_2I/g\text{-}C_3N_4$ heterojunction. The removal efficiency was significantly improved by using *t*-$PbBiO_2I/g\text{-}C_3N_4$. Catalytic performance observations indicated that the optimal reaction rate constant of $0.3259 \, h^{-1}$ can be obtained by using *t*-$PbBiO_2I/g\text{-}C_3N_4$; this is 9.1 and 13.7 times higher than those of the *t*-$PbBiO_2I$ and $g\text{-}C_3N_4$ photocatalysts, respectively. It is noted that the enhanced photocatalytic activity of *t*-$PbBiO_2I/g\text{-}C_3N_4$ corresponds to the formation of a heterojunction between *t*-$PbBiO_2I$ and $g\text{-}C_3N_4$; this is an effective phenomenon for suppressing photogenerated electron–hole recombination. Reactive $O_2{}^{\cdot-}$ plays a major role in the photocatalytic degradation of CV dyes, as evidenced by the quenching effect associated with scavengers. The method implemented in this study is of great significance for the synthesis of *t*-$PbBiO_2I/g\text{-}C_3N_4$ and photocatalytic degradation of CV dyes, and it can be used in future environmental pollution control applications.

CRediT authorship contribution statement

Li-Wen Chen: Data curation, Investigation, Writing - original draft, Writing - review & editing, Methodology. **Hung-Lin Chen:** Methodology, Validation, Investigation, Software, Methodology. **Chung-Shin Lu:** Writing - review & editing. **Shiuh-Tsuen Huang:** Writing - review & editing, Methodology. **Tsung-Wen Yeh:** Writing - review & editing. **Chiing-Chang Chen:** Supervision, Conceptualization, Visualization, Writing - review & editing, Validation.

Declaration of Competing Interest

The authors declare that they have no known competing financial interests or personal relationships that could have appeared to influence the work reported in this paper.

Acknowledgment

Appendix A. Supplementary data

Supplementary material related to this article can be found, in the online version, at doi:https://doi.org/10.1016/j.cattod.2020.06.015.

References

[1] M.R. Hoffmann, S.T. Martin, W. Choi, D.W. Bahnemann, Environmental applications of semiconductor photocatalysis, Chem. Rev. 95 (1995) 69–96.

[2] A. Kubacka, M. Fernández-García, G. Colón, Advanced nanoarchitectures for solar photocatalytic applications, Chem. Rev. 112 (2012) 1555–1614.

[3] S.T. Huang, Y.R. Jiang, S.Y. Chou, Y.M. Dai, C.C. Chen, Synthesis, characterization, photocatalytic activity of visible-light-responsive photocatalysts BiO_xCl_y/BiO_mBr_n by controlled hydrothermal method, J. Mol. Catal. A: Chem. 391 (2014) 105–120.

[4] H. Cheng, B. Huang, Y. Dai, Engineering BiOX (X = Cl, Br, I) nanostructures for highly efficient photocatalytic applications, Nanoscale 6 (2014) 2009–2026.

[5] Z. Chen, H. Jiang, W. Jin, C. Shi, Enhanced photocatalytic performance over $Bi_4Ti_3O_{12}$ nanosheets with controllable size and exposed {001} facets for Rhodamine B degradation, Appl. Catal. B: Environ. 180 (2016) 698–706.

[6] J.A. Seabold, K.S. Choi, Efficient and stable photo-oxidation of water by a bismuth vanadate photoanode coupled with an Iron oxyhydroxide oxygen evolution catalyst, J. Am. Chem. Soc. 134 (2012) 2186–2192.

[7] W. Wei, Y. Dai, B.B. Huang, First-principles characterization of Bi-based photocatalysts: $Bi_{12}TiO_{20}$, $Bi_2Ti_2O_7$, and $Bi_4Ti_3O_{12}$, J. Phys. Chem. C 113 (2009) 5658–5663.

[8] M. Batuk, D. Batuk, A.A. Tsirlin, D.S. Filimonov, Layered oxychlorides $[PbBiO_2]A_{n+1}BnO_{3n-1}Cl_2$ (A = Pb/Bi, B = Fe/Ti): intergrowth of the hematophanite and sillen phases, Chem. Mater. 27 (2015) 2946–2956.

[9] H.P. Lin, W.W. Lee, S.T. Huang, L.W. Chen, T.W. Yeh, J.Y. Fu, C.C. Chen, Controlled hydrothermal synthesis of PbBiO2Br/BiOBr heterojunction with enhanced visible-driven-light photocatalytic activities, J. Mol. Catal. A Chem. 417 (2016) 168–183.

[10] Y. Yu, Y. Gu, W. Zheng, Y. Ding, Y. Cao, New type photocatalyst PbBiO2Cl: materials design and experimental validation, J. Phys. Chem. C 119 (2015)

28190–28193.

[11] F.Y. Liu, Y.R. Jiang, C.C. Chen, W.W. Lee, Novel synthesis of PbBiO₂Cl/BiOCl nanocomposite with enhanced visible-driven-light photocatalytic activity, Catal. Today 300 (2018) 112–123.

[12] B. Wang, J. Di, P.F. Zhang, J.X. Xia, S. Dai, H.M. Li, Ionic liquid-induced strategy for porous perovskite-like PbBiO₂Br photocatalysts with enhanced photocatalytic activity and mechanism insight, Appl. Catal. B: Environ. 206 (2017) 127–135.

[13] S. Yin, T. Wu, M. Li, J. Di, M. Ji, B. Wang, Y. Chen, J. Xia, H. Li, Controllable synthesis of perovskite-like PbBiO₂Cl hollow microspheres with enhanced photocatalytic activity for antibiotic removal, CrystEngComm 19 (2017) 4777–4788.

[14] S. Yin, M. Li, W. Fan, Y. Ding, T. Wu, J. Di, M. Ji, J. Xia, H. Li, Controlled synthesis of novel PbBiO₂I microsphere structure towards photocatalytic degradation of bisphenol A, Res. Chem. Intermed. (2018), https://doi.org/10.1007/s11164-018-3461-6.

[15] H. Suzuki, H. Kunioku, M. Higashi, O. Tomita, D. Kato, H. Kageyama, R. Abe, Lead bismuth oxyhalides PbBiO₂X (X = Cl, Br) as visible-light-Responsive photocatalysts for water oxidation: role of lone-pair electrons in valence band engineering, Chem. Mater. 30 (2018) 5862–5869.

[16] J. Pan, Z. He, J. Su, R. Chen, B. Tang, Preparation and optical properties of Ni-doped PbBiO₂Br nanoparticles, Mater. Res. Express 6 (2019) 115042.

[17] Y. Yu, S. Huang, Y. Gu, S. Yan, Z. Lan, W. Zheng, Y. Cao, Study of PbBiO₂X (X = Cl, Br and I) square nanoplates with efficient visible photocatalytic performance, Appl. Surf. Sci. 428 (2018) 844–850.

[18] S. Rau, B. Scḧafer, D. Gleich, E. Anders, M. Rudolph, M. Friedrich, H. G̈orls, W. Henry, J.G. Vos, Ein supramolekularer Photokatalysator zur Erzeugung von Wasserstoff und zur selektiven Hydrierung von Tolan, Angew. Chem. 118 (2006) 6361–6364.

[19] H. Suzuki, M. Higashi, H. Kunioku, R. Abe, A. Saeki, Photoconductivity–lifetime product correlates well with the photocatalytic activity of oxyhalides Bi4TaO₈Cl and PbBiO₂Cl: an approach to boost their O₂ evolution rates, ACS Energy Lett. 4 (2019) 1572–1578.

[20] Y. Xia, Z. He, J. Su, K. Hu, Polyacrylamide gel synthesis and photocatalytic performance of PbBiO₂Br nanosheets, Mater. Lett. 241 (2019) 64–67.

[21] S. F̈uldner, P. Pohla, H. Bartling, S. Dankesreiter, R. Stadler, M. Gruber, A. Pfitzner, B. K̈onig, Selective photocatalytic reductions of nitrobenzene derivatives using PbBiO₂X and blue light, Green Chem. 13 (2011) 640–643.

[22] B. Wang, J. Di, L. Lu, S. Yan, G. Liu, Y. Ye, H. Li, W. Zhu, H. Li, J. Xia, Sacrificing ionic liquid-assisted anchoring of carbonized polymer dots on perovskite-like PbBiO₂Br for robust CO₂ photoreduction, Appl. Catal. B: Environ. 254 (2019) 551–559.

[23] H. Guo, C.G. Niu, D.W. Huang, N. Tang, G.M. Zeng, Integrating the plasmonic effect and p-n heterojunction into a novel Ag/Ag₂O/PbBiO₂Br photocatalyst: broadened light absorption and accelerated charge separation co-mediated highly efficient visible/NIR light photocatalysis, Chem. Eng. J. 360 (2019) 349–363.

[24] Y. Xia, Z. He, J. Su, K. Hu, Construction of novel Cu₂O/PbBiO₂Br composites with enhanced photocatalytic activity, J. Mater. Sci. Mater. Electr. 30 (2019) 9843–9854.

[25] S. Li, X. Wang, Y. Xu, H. Yang, F. Wei, X. Liu, The excellent photocatalytic synergism of PbBiO₂Br/UiO-66-NH₂ composites via multiple coupling effects, RSC Adv. 6 (2016) 89907–89915.

[26] X. Li, J. Wang, D. Xu, Z. Sun, Q. Zhao, W. Peng, Y. Li, G. Zhang, F. Zhang, X. Fan, NbSe₂ nanosheet supported PbBiO₂Br as a high performance photocatalyst for the visible light-driven asymmetric alkylation of aldehyde, ACS Sustain. Chem. Eng. 3 (2015) 1017–1022.

[27] F.Y. Liu, J.H. Lin, Y.M. Dai, L.W. Chen, S.T. Huang, T.W. Yeh, J.L. Chang, C.C. Chen, Preparation of perovskites PbBiO₂I/PbO exhibiting visible-light photocatalytic activity, Catal. Today 314 (2018) 28–41.

[28] Q. Hu, S. Yin, Y. Ding, T. Wu, H. Li, Ultrathin graphitic carbon nitride modified PbBiO₂Cl microspheres with accelerating interfacial charge transfer for the photodegradation of organic contaminants, Colloids Surf. A 582 (2019) 123804.

[29] B. Wang, J. Di, G. Liu, S. Yin, J. Xia, Q. Zhang, H. Li, Novel mesoporous graphitic carbon nitride modified PbBiO₂Br porous microspheres with enhanced photocatalytic performance, J. Colloid Interface Sci. 507 (2017) 310–322.

[30] Hai Guo, Cheng-Gang Niu, Xiao-Ju Wen, Lei Zhang, Guang-Ming Zeng, Construction of highly efficient and stable ternary AgBr/Ag/PbBiO₂Br Z-scheme photocatalyst under visible light irradiation: performance and mechanism insight, J. Colloid Interface Sci. 513 (2018) 852–865.

[31] A.H. Lee, Y.C. Wang, C.C. Chen, Composite photocatalyst, tetragonal lead bismuth oxyiodide/bismuth oxyiodide/graphitic carbon nitride: synthesis, characterization, and photocatalytic activity, J. Col. Interface Sci. 533 (2019) 319–332.

[32] Y.C. Wang, A.H. Lee, C.C. Chen, Perovskite-like photocatalyst, PbBiO₂Br/PbO/g-C₃N₄: synthesis, characterization, and visible-light-driven photocatalytic activity, J. Taiwan Inst. Chem. Eng. 93 (2018) 315–328.

[33] B. Wang, G. Liu, B. Ye, Y. Ye, W. Zhu, S. Yin, J. Xia, H. Li, Novel CNT/PbBiO₂Br hybrid materials with enhanced broad spectrum photocatalytic activity toward ciprofloxacin (CIP) degradation, J. Photochem. Photobiol. A: Chem. 382 (2019) 111901.

[34] M. Li, S. Yin, T. Wu, J. Di, M. Ji, B. Wang, Y. Chen, J. Xia, H. Li, Controlled preparation of MoS₂/PbBiO₂I hybrid microspheres with enhanced visible-light photocatalytic behavior, J. Colloid Interface Sci. 517 (2018) 278–287.

[35] Y.R. Jiang, H.P. Lin, W.H. Chung, Y.M. Dai, W.Y. Lin, C.C. Chen, Controlled hydrothermal synthesis of BiOₓClᵧ/BiOₘInₙ composites exhibiting visible-light photocatalytic degradation of crystal violet, J. Hazard. Mater. 283 (2015) 787–805.

[36] L.S. Zhang, K.H. Wong, H.Y. Yip, C. Hu, J.C. Yu, C.Y. Chan, P.K. Wong, Effective photocatalytic disinfection of E. coli K-12 using AgBr−Ag−Bi₂WO₆ nanojunction system irradiated by visible light: the role of diffusing hydroxyl radicals, Environ. Sci. Technol. 44 (2010) 1392–1398.

[37] M.C. Yin, Z.S. Li, J.H. Kou, Z.G. Zou, Mechanism investigation of visible light-induced degradation in a heterogeneous TiO₂/eosin Y/rhodamine B system, Environ. Sci. Technol. 43 (2009) 8361–8366.

[38] S.G. Meng, D.Z. Li, M. Sun, W.J. Li, J.X. Wang, J. Chen, X.Z. Fu, G.C. Xiao, Sonochemical synthesis, characterization and photocatalytic properties of a novel cube-shaped CaSn(OH)₆, Catal. Commun. 12 (2011) 972–975.

[39] G. Li, K.H. Wong, X. Zhang, C. Hu, J.C. Yu, R.C.Y. Chan, P.K. Wong, Degradation of Acid Orange 7 using magnetic AgBr under visible light: the roles of oxidizing species, Chemosphere 76 (2009) 1185–1191.

[40] Y.R. Jiang, S.Y. Chou, J.L. Chang, S.T. Huang, H.P. Lin, C.C. Chen, Hydrothermal synthesis of bismuth oxybromide-bismuth oxyiodide composites with highly visible light photocatalytic performance for the degradation of CV and phenol, RSC Adv. 5 (2015) 30851–30860.

[41] S.C. Yan, Z.S. Li, Z.G. Zou, Photodegradation performance of g-C₃N₄ fabricated by directly heating melamine, Langmuir 25 (2009) 10397–10401.

[42] H.L. Chen, W.W. Lee, W.H. Chung, H.P. Lin, Y.J. Chen, Y.R. Jiang, W.Y. Lin, C.C. Chen, Controlled hydrothermal synthesis of bismuth oxybromides and their photocatalytic properties, J. Taiwan Inst. Chem. Eng. 45 (2014) 1892–1909.

[43] Y. Li, H. Zhang, P. Liu, D. Wang, Y. Li, H. Zhao, Cross-linked g-C₃N₄/rGO nanocomposites with tunable band structure and enhanced visible light photocatalytic activity, Small 9 (2013) 3336–3344.

[44] J. Zhang, M. Zhang, G. Zhang, X. Wang, Harnessing protein symmetry for enzyme design, ACS Catal. 2 (2012) 940–948.

[45] Y.R. Jiang, S.Y. Chou, J.L. Chang, S.T. Huang, H.P. Lin, C.C. Chen, Hydrothermal synthesis of bismuth oxybromide-bismuth oxyiodide composites with highly visible light photocatalytic performance for the degradation of CV and phenol, RSC Adv. 5 (2015) 30851–30860.

[46] S.Y. Chou, W.H. Chung, L.W. Chen, Y.M. Dai, W.Y. Lin, J.H. Lin, C.C. Chen, A series of BiOₓIᵧ/GO photocatalysts: synthesis, characterization, activity, and mechanism, RSC Adv. 6 (2016) 82743–82758.

[47] J. Zhang, M. Zhang, G. Zhang, X. Wang, Synthesis of carbon nitride semiconductors in sulfur flux for water photoredox catalysis, ACS Catal. 2 (2012) 940–948.

[48] W.W. Lee, C.S. Lu, C.W. Chuang, Y.J. Chen, J.Y. Fu, C.W. Siao, C.C. Chen, Synthesis of bismuth oxyiodides and their composites: characterization, photocatalytic activity, and degradation mechanisms, RSC Adv. 5 (2015) 23450–23463.

[49] B.P. Barbero, L.E. Cadus, V₂O₅–SmVO₄ mechanical mixture: oxidative dehydrogenation of propane, Appl. Catal. A 237 (2002) 263–273.

[50] H.J. Fan, C.S. Lu, W.L.W. Lee, M.R. Chiou, C.C. Chen, Mechanistic pathways differences between P25-TiO₂ and Pt-TiO₂ mediated CV photodegradation, J. Hazard. Mater. 185 (2011) 227–235.

[51] F. Dong, Y. Sun, M. Fu, Z. Wu, S.C. Lee, Room temperature synthesis and highly enhanced visible light photocatalytic activity of porous BiOI/BiOCl composites nanoplates microflowers, J. Hazard. Mater. 219–220 (2012) 26–34.

[52] A. Chatzitakis, C. Berberidou, I. Paspaltsis, G. Kyriakou, T. Sklaviadis, I. Poulios, Photocatalytic degradation and drug activity reduction of chloramphenicol, Water Res. 42 (2008) 386–394.

[53] N.M. Dimitrijevic, B.K. Vijayan, O.G. Poluektov, T. Rajh, K.A. Gray, H. He, P. Zapol, Role of water and carbonates in photocatalytic transformation of CO₂ to CH₄ on titania, J. Am. Chem. Soc. 133 (2011) 3964–3971.

[54] H. Li, Y. Zhou, W. Tu, J. Ye, Z. Zou, State-of-the-art progress in diverse heterostructured photocatalysts toward promoting photocatalytic performance, Adv. Funct. Mater. 25 (2015) 998–1013.

[55] Z. Li, J. Feng, S. Yan, Z. Zou, Solar fuel production: strategies and new opportunities with nanostructures, Nano Today 10 (2015) 468–486.

[56] H. Falco´n, J.A. Barbero, J.A. Alonso, M.J. Mart´ınez-Lope, J.L.G. Fierro, SrFeO₃.δ perovskite oxides: chemical features and performance for methane combustion, Chem. Mater. 14 (2002) 2325–2333.

[57] Y. Tian, B. Chang, J. Lu, J. Fu, F. Xi, X. Dong, Hydrothermal synthesis of graphitic carbon nitride–Bi₂WO₆ heterojunctions with enhanced visible light photocatalytic activities, ACS Appl. Mater. Interfaces 5 (2013) 7079–7085.